UHASSELT
KNOWLEDGE IN ACTION

Maastricht University

# Faculty of Medicine and Life Sciences
## *School for Life Sciences*
## Master of Biomedical Sciences

***Master's thesis***

***Fabrication of a diamond-based impedance sensor to monitor cyanobacterial growth***

**Nora Colson**

Thesis presented in fulfillment of the requirements for the degree of Master of Biomedical Sciences, specialization Bioelectronics and Nanotechnology

**SUPERVISOR :**

dr. Rozita ROUZBAHANI BAYATANI

**2021**
**2022**

Transnational University Limburg is a unique collaboration of two universities in two countries: the University of Hasselt and Maastricht University.

UHASSELT
KNOWLEDGE IN ACTION

**www.uhasselt.be**
Universiteit Hasselt
Campus Hasselt:
Martelarenlaan 42 | 3500 Hasselt
Campus Diepenbeek:
Agoralaan Gebouw D | 3590 Diepenbeek

UHASSELT
KNOWLEDGE IN ACTION

Maastricht University

# Faculty of Medicine and Life Sciences
## *School for Life Sciences*
## Master of Biomedical Sciences

***Master's thesis***

***Fabrication of a diamond-based impedance sensor to monitor cyanobacterial growth***

**Nora Colson**

Thesis presented in fulfillment of the requirements for the degree of Master of Biomedical Sciences, specialization Bioelectronics and Nanotechnology

**SUPERVISOR :**
dr. Rozita ROUZBAHANI BAYATANI

# Fabrication of diamond-based impedance sensor to monitor cyanobacterial growth

Colson N., Ahmed E. and Rouzbahani R.

Wide Band Gap Materials research group, IMO-IMOMEC, Hasselt University, Campus Diepenbeek, Wetenschapspark 1-B-3590 Diepenbeek

*Running title: *Impedance sensor to monitor cyanobacterial growth*

To whom correspondence should be addressed: Dr. Rouzbahani Rozita Tel: +32 (11) 26 88 47; Email: rozita.rouzbahani@uhasselt.be

**Keywords:** electrochemical impedance spectroscopy (EIS), biofilm, cyclic voltammetry (CV), diamond, interdigitated transducer electrodes, biosensor

## ABSTRACT

**The increasing use of cyanobacteria in biotechnological applications requires careful monitoring of the growth and biofilm formation of these species. Due to the labor-intensiveness and high cost of conventional growth monitoring techniques, there is an interest in new, alternative sensing approaches for this purpose. In this work, the development of a diamond-based impedance sensor to monitor cyanobacterial growth is described. For this sensor, different types of electrodes were fabricated and tested. The envisioned sensor contained interdigitated transducing electrodes (IDTs), as these are most commonly used for impedance-based sensors to monitor cell growth. However, as an initial test of the setup, cyclic voltammetry (CV) and electrochemical impedance spectroscopy (EIS) were performed using boron-doped diamond film electrodes. Titanium IDTs were successfully fabricated as the second type of electrodes and tested in EIS measurements. The other exploited approaches to obtain IDTs, require additional optimization before being tested in the sensor. Both the boron-doped diamond film electrodes and titanium IDTs were tested with baker's yeast as a proof of principle. In the CV measurements, a peak potential shift towards lower values was observed with increasing yeast concentration. The Nyquist plots of EIS spectra of both types of electrodes showed the tendency to form a semicircle of which the radius, i.e. impedance, decreased with increasing yeast concentration. Although extensive circuit modeling and comparison between the different types of electrodes are needed to draw firm conclusions, the presented results lay the first cornerstones for an alternative impedance-based sensor to monitor (cyano)bacterial growth.**

## INTRODUCTION

Cyanobacteria, also known as blue-green algae, are a kind of prokaryotic, gram-negative, and abundantly present bacteria. Ever since the emergence of the earth billions of years ago, cyanobacteria have played a major role in its evolution (1). Moreover, cyanobacteria have gained a lot of interest over the past years due to their numerous potential applications in the biotechnological industry, ranging from cyanobacterial biofertilizers to cyanobacterial emulsifiers and solar hydrogen bioreactors (2,3) One specific strain of cyanobacteria that has gained a lot of interest within numerous biotechnological applications is *Limnospira indica* PCC 8005. This type of cyanobacteria, having a high nutritive value, is being used in the biopharmaceutical industry but can also be used for energy harvesting and solar fuel production (4). Approximately three decades ago, *Limnospira indica* was recognized as a primary candidate for biological life support systems in future space stations and missions by the European Space Agency (5,6). In a future project, this potential will be investigated through the fabrication of photoelectrochemical cells equipped with a cyanobacterial biofilm to produce hydrogen and oxygen in space missions. Nevertheless, using these types of bacterial strains in biotechnological applications requires careful monitoring and controlling of their growth process in order to study

and optimize the biofilm formation, growth kinetics, biomass, and metabolite production (7).

Conventionally, in microbiological research, the growth of microorganisms, like bacteria, in culture is assessed through analytical parameters such as cell number, optical density, oxygen consumption, or the pH of the growth medium. These approaches are either classified as direct or indirect methods and although these methods have been used in this field for ages, both types of methods are associated with serious drawbacks (8). Direct methods, mainly based on colony counting, are characterized by their labor-intensive nature and inaccurate results (9). Indirect methods, such as spectrophotometry, enable the researcher to generate more reliable results but require expensive infrastructure, and trained personnel and are labor-intensive in case of continuous monitoring as it requires multiple samplings. As a consequence of these drawbacks, there is an interest in the development of new methods to monitor (cyano)bacterial growth.

Electrochemical quantification methods like cyclic voltammetry (CV) and impedance spectroscopy (EIS) are suitable techniques for this purpose and do not require sophisticated infrastructure (10,11). Both electroanalytical techniques monitor the electrical response of a chemical system, more specifically redox characteristics in CV and charge carrier dynamics in EIS.

In CV, a range of potentials is applied to the three-electrode setup and the resulting current is recorded, generating an I-V curve. Depending on the electroactive compound, oxidation and reduction peaks are observed at the working potential of the compound.

In impedance spectroscopy, a low amplitude alternating voltage with a range of frequencies is applied and the resulting impedance, or the ratio of the applied alternating potential and the resulting alternating current, is measured. The principle of electrochemical impedance spectroscopy has been used in numerous various research and development areas for a wide range of applications in electrical, electronic, and electrochemical engineering, like corrosion rate and state-of-charge determination in battery research (12). Nevertheless, the principle of EIS is also increasingly being used in impedance-based sensors for cell-growth monitoring and pathogen detection (13–16). This is mostly because impedance is still known as one of the most powerful methods to monitor cell growth (13). Most studies, however, are focused on the detection and growth monitoring of pathogenic bacteria that pose a potential health threat to our society, such as *Salmonella enterica*, instead of beneficial bacteria such as cyanobacteria for biotechnological applications (17).

As mentioned before, a major advantage of electrochemical measurements is their simple setup requirements. Usually, a three-electrode setup is deployed in an electrochemical cell, used to house the electrochemical reactions. Various materials have been used as working electrodes in the past, however, one promising material that has gained considerable interest for sensing applications in the last decades is synthetic diamond (18).

The complete $sp^3$ hybridization of carbon in diamond gives rise to many exceptional properties like its hardness, very high thermal conductivity, and extremely high electrical resistivity (13,19); intrinsic nanocrystalline diamond (NCD) is a wide band gap semiconductor with a band gap of 5.47 eV at 300 K (20). In this regard, intrinsic diamond is not suitable for electrochemical measurements, however, dopant impurities can be added to modify the electrical properties of the diamond film, leaving it suitable for electrode applications. On top of this, diamond is also well known for its biocompatibility (13), which is crucial when using this material as a working electrode in the electrochemical sensing of biological material or species.

While the growth of synthetic diamond used to happen under high pressure, high temperature (HPHT) conditions, currently, diamond is mainly produced from gas-phase carbon using chemical vapor deposition (CVD) techniques at low pressures. In these techniques, a single crystal diamond or a non-diamond substrate, nucleated with nanodiamonds, is exposed to $H_2$-rich plasma containing $CH_4$, as the carbon source required to form the desired diamond film. As mentioned before, the introduction of dopants, such as boron or phosphorus, to the gas mixture, leads to the formation of an electrically conductive p- or n-type doped diamond layer. On top of this, the process of synthetic diamond deposition allows altering the duration and temperature during the process, leading to changes in the morphology, grain size,

and electrical properties of the obtained diamond film, which in turn influences the sensing properties of the material (21).

In 2019, *Prochàzka et al.* (13) used an NCD film under which titanium interdigitated transducing (IDT) electrodes were formed, in an impedance-based sensor for the real-time monitoring of stem cells. Before that, *Izàk et al.* (22) realized conductive IDT electrodes in the diamond film through the introduction of local conductive hydrogen-terminated regions separated by insulating oxygen-terminated regions. With this approach, the use of conventional metals, like the sensor in the work of *Prochàzka et al.* (13), was circumvented, which is beneficial due to the earlier mentioned biocompatible properties of diamond.

This work reports on the development of a similar impedance-based sensor to monitor cyanobacterial growth. The envisioned sensor contains conductive IDTs realized on top of a non-conductive, intrinsic diamond film. The intrinsic diamond serves as a biocompatible surface on which the cyanobacteria can form a biofilm. During this process, the impedance of the biofilm measured between the working and counter IDT provides an estimation of the thickness of the bacterial biofilm. In this way, the sensor will be able to monitor the bacterial biofilm formation over time, providing an alternative to the conventional bacterial growth monitoring techniques (**Figure 1**). Based on literature, it is assumed that the impedance of the system will decrease as the biofilm develops, mainly due to the increasing electron pool, contributing to higher conductivity between the biofilm and the electrode (23).

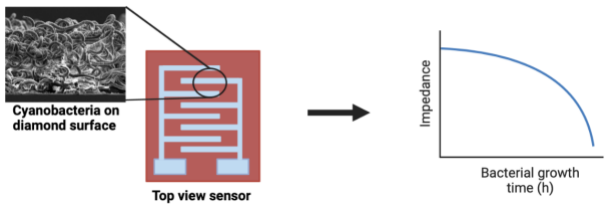


**Figure 1: Scheme of the envisioned sensor and its working principle.** The cyanobacterial biofilm formation takes place on the surface of the sensor and the monitoring of the change in impedance gives an estimation of the thickness of the biofilm over time.

However, since the fabrication of IDTs is challenging, different types of diamond-based electrodes were fabricated in this research, using various techniques. The first type of working electrodes fabricated were **boron-doped diamond films on a silicon substrate**. In a second approach, **titanium IDTs** were realized on top of an intrinsic NCD layer using photolithography. The third attempt to make the envisioned electrode comprised ink-jet printed nanodiamond seeding in the desired IDT pattern and subsequent boron-doped diamond growth, resulting in **boron-doped diamond IDTs on fused silica substrates**. Lastly, **conductive silver-based IDTs** were printed directly on top of an intrinsic diamond layer using a Voltera V-one printer.

Once finished, the electrodes were incorporated into a customized in-house built flow cell. For the electrochemical measurements, the contact pads were connected to an alternating current source and the extracted current and voltage of the system were recorded. As a first test of the developed flow cell and the potentiostat, the sensor was tested using vanillin as an electroactive compound on boron-doped diamond films, as this is a relatively well-established method in literature (24). Subsequently, the sensor was tested with the aforementioned types of electrodes, on a range of different concentrations of *Saccharomyces cerevisiae*, trivially known as baker's yeast. These cells are often used to mimic eukaryotic cell behavior in the fields of biotechnology, pharmacy, and biomedicine (25). In this case, however, they were used to mimic the behavior of a biofilm on the developed electrodes. *Saccharomyces cerevisiae* and cyanobacteria differ significantly in many aspects. First of all, yeast is considered a eukaryotic organism while cyanobacteria belong to the prokaryotes, moreover, the cell walls of both species are made up of chitin and murein respectively (26). Nevertheless, both species show a lot of similarities, like their unicellular structure, and more important for this research, the ability to adhere to the surface, leading to the formation of a biofilm (27,28). In this regard, yeast was used as a proof of principle for the future use of the developed sensor for cyanobacterial growth monitoring.

## EXPERIMENTAL PROCEDURES

*Reagentia* – Phosphate buffered saline (PBS) powder from Sigma-Aldrich was dissolved in deionized (DI) water until a concentration of 0.01 M was reached at a pH of 7.4. For the analytes,

commercially available vanillin (Imperial) and *Saccharomyces cerevisiae* (baker's yeast, Bruggeman) were used. For both analytes, the concentration range of 0.01 M to 0.05 M was prepared in PBS.

**Pre-treatment of substrates**

*Cleaning of substrates* – In this research, three different procedures were used to ensure the removal of surface contaminants from the substrates prior to diamond CVD growth.

In oxygen cleaning, the substrates were exposed to oxygen gas discharge plasma for a duration of 90 s at 200 W with an $O_2$ flux of 50 sccm.

Cleaning with $CF_4$ was performed in order to obtain a hydrophobic surface. In this case, the substrates were exposed to $CF_4$ plasma for 3 min at 300 W with an Argon flux of 42 sccm.

The third cleaning approach consisted of exposure to ozone with a mercury vapor lamp generating UV light at both 185 nm and 254 nm (PSD series, Novascan) for 1 h.

*Seeding of substrates* – Pre-treatment also included seeding of nanodiamonds on the surface, to ensure the formation of a smooth and homogenous diamond film. In this research, three different seeding techniques were exploited.

In spin seeding, drop-casting of an aqueous colloidal solution of nanodiamond particles (0.267 g/L, NanoCarbon Institute Co., Ltd.) on the cleaned substrates was followed by a 15 s flushing step with DI water and subsequent spin-drying at 4000 rpm.

For the second approach called spray seeding, an ultrasonic spray coater (Exacta Coat, Sono-Tek cooperation) equipped with an impact nozzle was used. Once the substrates reached a temperature of 90 °C on the hotplate, they were sprayed with an aqueous seeding colloid (0.05 g/l single-digit nanodiamonds, PlasmaChem GMbH). The seeding colloid was atomized with a power of 4 W at a liquid feed flow rate of 0.25 ml/min. Subsequently, by using a nitrogen carrier shroud gas and a pressure of 9 kPa, the droplets were transported over a distance of 5 cm. The nozzle trajectory was repeated 160 times at a velocity of 50 mm/s.

Ink-jet printing of nanodiamond seeds was performed as a third approach. Prior to this technique, the samples were cleaned by exposure to $CF_4$ plasma, generating a hydrophobic surface. Printing of the nanodiamond seeds in the desired pattern was carried out using a Fujifilm Dimatix materials printer. The ink was made by mixing Single-Digit NanoDiamonds (SDND, Plasmachem) with particle sizes of 5-15 nm with 55% ethylene glycol, 25% ethanol, and 20% DI water. To prevent clogging of the nozzle due to diamond nanoparticle clusters, the ink was centrifuged for 30 min at 5000 g prior to printing. The pattern was seeded with ink drops of 1 pl with a drop spacing of 15 µm at a frequency of 2 kHz. During the printing process, the temperature was kept at 60 °C.

**CVD of diamond layers**

*Intrinsic diamond* – Intrinsic diamond was deposited in a linear antenna (LA) pulsed microwave plasma-enhanced CVD system. The deposition conditions for this process were the following: microwave power 2800 W, pressure 0.22 Pa, gas mixture 138/4/8 sccm of $H_2/CH_4/CO_2$, and the stage was heated to a temperature of 400 °C.

*B-doped diamond* – B-doped diamond films were grown in an ASTeX 6500 CVD reactor using trimethyl boron ($B(CH_3)_3$) gas diluted in $H_2$ (1000 ppm) as a doping agent. During the deposition process, the total gas flux was 500 sccm ($H_2/CH_4$/ $B(CH_3)_3$= 395/5/100 sccm) and the B/C ratio in the gaseous phase was 20000 ppm. A working pressure of 5.3 kPa and a microwave power of 4000 W were used. The temperature during the process was kept around 700 °C, monitored with a Minolta/Land Cyclops 52 pyrometer, using an emissivity of 0.6.

*Characterization* – Raman spectroscopy was performed with a Horiba Jobin Yvon T64000 Raman spectrometer equipped with a CCD detector and a 488 nm Lexell SHG laser over the range of 1145-1799 $cm^{-1}$. Surface morphology characterization was done by scanning electron microscopy (SEM), using a FEI Quanta 200 FEG scanning electron microscope at 30 kV. For roughness determination, a Veeco NanoScope III MultiMode atomic force microscope (AFM) in tapping mode was used.

**Electrodes**

*B-doped diamond electrode* – As the first type of electrode, B-doped diamond electrodes were fabricated. These electrodes consist of a B-doped

NCD layer of 200 nm on top of a silicon (100-oriented) substrate (p-type, 1-20 Ω cm), deposited as mentioned in the section *"B-doped diamond"*.

*Titanium IDTs* – For biocompatibility purposes, fused silica substrates were overgrown with a 450 nm intrinsic NCD layer, using a linear antenna (LA) pulsed microwave plasma-enhanced CVD system as described in the section *"Intrinsic diamond"*. Subsequently, metal composite IDT electrodes with a width and gap electrode periodicity of 80 µm were formed on top of the diamond layer through photolithography followed by metal deposition and lift-off. Negative photoresist (NR9-3000PY, Futurrex, Inc.) was spin-coated on top of the diamond layer on the fused silica substrates at 4000 rpm for 40 s. After soft baking at 150 °C for 80 s, substrates were left to cool down to ambient temperature. To generate the desired pattern on the substrates, a soda-lime mask using chromium as optical blocking material to define the features of the mask was used. Subsequently to exposure of the photoresist layer through this mask to an ultraviolet (UV) light source (Xe arc lamp) using a Karl Suss mask aligner (MA55), the samples were baked on a hotplate at 100 °C for another 80 s. Once the substrates reached room temperature, the photoresist in the unexposed regions was washed away through a 30 s developing step in RD6 (Futurrex, Inc.). Subsequently, the samples were rinsed with DI water and dried using nitrogen gas.

Prior to metal sputtering and to improve metal adhesion to the photoresist uncoated surfaces, ozone treatment was performed for 2 hours. Subsequently, using a home-build direct current pulsed sputtering system, a titanium layer of 50 nm was deposited on the surfaces at 150 W. During this process, the argon flux was kept constant at 50 sccm and the working pressure was 0.56 Pa. Finally, to discard the metal in between the patterned IDTs, the substrate was left in acetone for 60 s, followed by 5 s in an ultrasonic bath.

*B-doped diamond IDTs* – For the third type of IDTs fabricated, a collaboration with the research group of prof. dr. ir. Wim Deferme was started. Their group provided fused silica substrates with the desired IDT pattern with a width/gap of 250/150 µm, seeded by ink-jet printing. To generate B-doped diamond IDTs, diamond deposition using the same conditions as mentioned in the section *"B-doped diamond"* was performed.

*Printed conductive IDTs* – In collaboration with the University of Bergen (Norway), conductive IDTs were printed on top of an intrinsic diamond film. For this purpose, an intrinsic diamond film of 270 nm thickness was grown on fused silica substrates in a LA CVD reactor, using the same conditions as specified in the section "*Intrinsic diamond".* The pre-treatment, prior to diamond deposition consisted of $O_2$ cleaning and spin-seeding. Using a Voltera V-one printed circuit board (PCB) printer, conductive silver-based contacts with a width/gap spacing of 440 µm/150 µm were printed on top of the intrinsic diamond layer with Flex 2 ink from Voltera.

**Electrochemical measurements**

*Apparatus* – The electrochemical measurements were carried out using a three-electrode setup in combination with two slightly different in-house designed flow cells (**Figure 2**). However, both flow cells consisted of the same materials and were assembled in the same way, only the PCB used differed slightly.

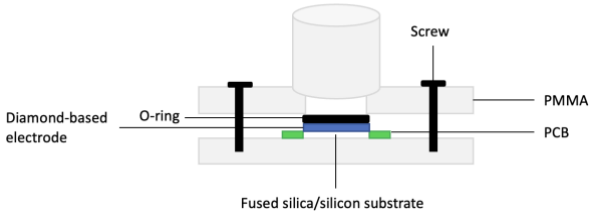


**Figure 2: Scheme of the fabricated flow cell.** The different developed electrodes were embedded in a printed circuit board (PCB). Depending on the type of electrode, the diamond-containing layer was deposited on top of a fused silica or silicon substrate. For the insulating housing around the PCB with the working electrode, two polymethylmethacrylate (PMMA) plates were screwed together. To seal the cell watertight a rubber O-ring was used.

In this setup, a silver/silver chloride (3 M KCl) reference electrode was used together with the different types of working electrodes fabricated during this research. For the measurements with the boron-doped diamond electrodes, the working electrode was immobilized on a PCB using conductive silver paste. This allowed applying a potential from the back of the substrate. Exposure of the electrolyte to silver paste was prevented to avoid contamination of the CV by the induction of a silver peak. For these electrodes, the stainless-

steel fluid outlet of the cell, which was in contact with the electrolyte was used as a counter electrode. The three electrodes were connected to the potentiostat using crocodile clamps (SensitBT, Palmsens).
The IDT electrodes were immobilized on the PCB using carbon tape and in this case, the potential was applied from the top of the substrate. The working and counter IDT electrodes on the substrate were connected to two contact pads on the PCB which were subsequently connected to the potentiostat. The potentiostat was connected to a laptop equipped with the required software (PStrace).

*Cyclic voltammetry* – CV of the different electroactive compounds was performed at a scan rate of 0.05 V/s. The potential range was set to the maximum range of the device, being -1.2 V to 1.2 V and the step size was set to 0.01 V.

*Electrochemical impedance spectroscopy* – To ensure that the capacitive current had decayed, the equilibration time was set to 5 s. The spectra were recorded at a fixed potential with an amplitude of 0.01 V. To prevent unreliable data due to instability of the system during long measurements, the lowest chosen frequency was 0.1 Hz. Resulting in the frequency range of 0.1 Hz – 20 kHz.

## RESULTS AND DISCUSSION

*The effect of spin and spray seeding on intrinsic NCD film formation* – The nucleation step prior to CVD is vital to obtain smooth, homogeneous, and uniform NCD films. Usually, this is done by spin seeding, however, spray seeding of the substrates provides a less laborious and time-consuming alternative for this process. To assess the influence of these different seeding techniques on the NCD film formation, SEM was performed after intrinsic NCD film deposition in the LA CVD reactor (**Figure 3**). The average grain sizes for the spin seeded and spray seeded samples were similar, being 226 nm and 210 nm respectively (**Figure 3A and B**). Nevertheless, AFM measurements on both samples showed a significant difference in roughness between the spin seeded and spray seeded samples with average roughness values of 9 nm and 18 nm respectively (**Figure 3C and D**). The presence of diamond was confirmed in both samples through Raman spectroscopy with a typical sharp $sp^3$ peak at 1333 $cm^{-1}$ and 1332 $cm^{-1}$ for the spin seeded and spray seeded samples respectively (**Figure 3E)**(29).
Based on these results, it can be concluded that the major difference induced by spray seeding can be found in the roughness of the resulting diamond layer. Unpublished data from our collaborator indicates that the increased roughness is due to the fact that more seeds need to be deposited on the surface using spray seeding to achieve a closed diamond film. This leads to the stacking of several seeds on top of each other, resulting in a rougher surface before the diamond film formation, which in turn generates a rougher diamond film after growth.

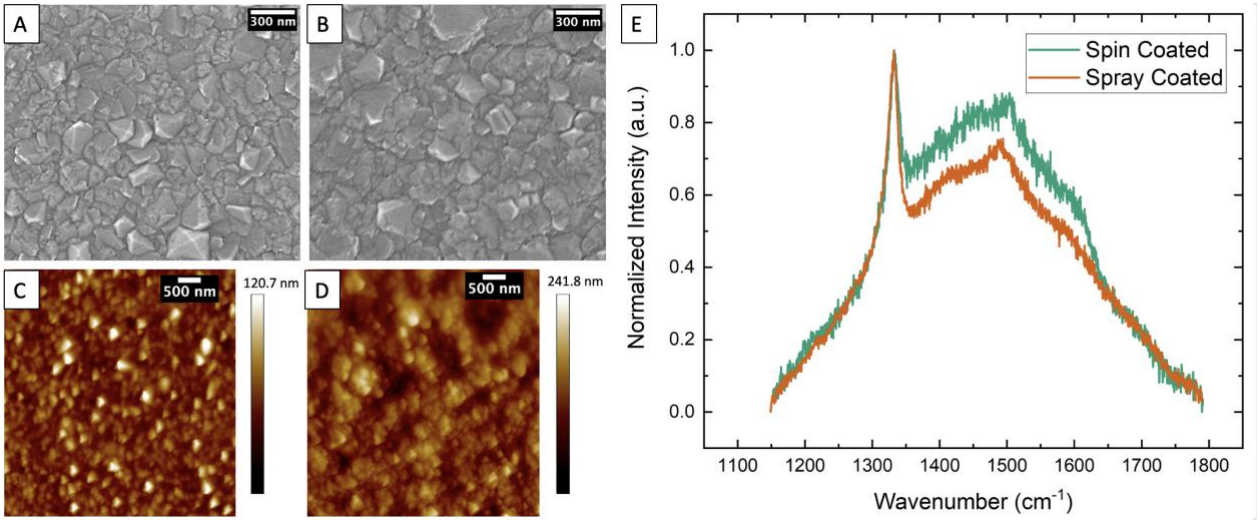


**Figure 3: Morphology comparison of spin and spray seeded samples.** Similar grain sizes were seen for the spin seeded (A) and spray seeded (B) samples in the obtained SEM images. However, the AFM images showed an increase in roughness in the spray seeded samples (D) compared to the spin seeded samples (C). The Raman spectra of both samples (E) were similar and showed the typical $sp^3$ peak around 1330 $cm^{-1}$.

**Electrode fabrication**

*B-doped diamond electrode* – When using B-doped diamond (BDD) films for electrochemical measurements, a few important considerations must be taken into account regarding the material properties of the BDD electrode. For this reason, the obtained BDD films were characterized using various methods. For surface morphology assessment, SEM was used in conjunction with AFM to estimate the grain size and surface roughness of the film as these play an important role in the formation of the double-layer capacitance of the material during electrochemical measurements (19). The SEM images (**Supplementary figure 1**) indicated an average grain size of 261 nm, making the material classified as nanocrystalline diamond (19). Using AFM an average roughness value of 10.4 nm was found (**Supplementary figure 2**). In the Raman spectrum of the obtained BDD film, two peaks were observed (**Supplementary figure 3**). The peak at 1332 $cm^{-1}$ confirmed the presence of pure diamond in the film, and the broad peak at 1550 $cm^{-1}$ can be attributed to the presence of non-diamond carbons, which are $sp^2$ hybridized. The incorporation of non-diamond carbon atoms is almost unavoidable when growing BDD films and makes the electrode less electrocatalytically inert, resulting in a reduced solvent window and decreased limits of detection (19).

Since pure diamond is a very wide band gap semiconductor, it is important to have an estimation of the boron dopant density of the BDD electrodes. As mentioned before, boron doping introduces p-type acceptors (holes) into the lattice, which in turn leads to semi-metallic properties. Depending on the level of boron doping the charge carrier availability for electrochemical measurements changes. For the BDD films fabricated in this work, the ratio of $TMB/CH_4$ was 20000 ppm. However, this value only provides a qualitative indication that the diamond film is sufficiently doped to behave metal-like. Quantitative values, expressed in the number of boron atoms per $cm^3$ can be obtained using secondary ion mass spectrometry (SIMS), but this could not be achieved within the limited timeframe of this work.

Another important property of BDD electrodes is the surface termination. This does not only affect the wetting properties of the electrode but also leads to electrostatic interactions which can raise or lower the energy levels of the valence and conduction bands, leading to negative or positive electron affinity respectively. The surface termination of the obtained diamond films in this research was investigated using water contact angle (CA) measurements (**Supplementary figure 4**) and a CA of 81° was found. For a diamond film obtained by CVD growth, hydrophobic surfaces, e.g. CA of 90° (30), are expected due to the hydrogen-terminated nature of the substrates. However, it is well-known that hydrogen-terminated BDD films oxidize slowly when exposed to ambient air, resulting in a decrease in CA (19). On top of this, there is evidence that increasing boron doping leads to more hydrophilic values (19). Nevertheless, since the CA is relatively close to the theoretically defined 90° for hydrophobic surfaces, it can be assumed that the BDD film is hydrogen-terminated. As mentioned before, this leads to negative electron affinity, resulting in surface conductivity during electrochemical measurements.

*Optimization photolithography for titanium IDTs* – Photolithography is the general name for a technique that allows a person to pattern thin films on a substrate through the use of light. The process of photolithography is challenging and requires numerous optimization steps depending on the desired pattern and materials used. For this research, the idea was to pattern titanium IDTs on an NCD surface. For the envisioned IDTs, a mask with width/gap distances ranging from 5 to 100 µm between the IDT "fingers" was developed. To use these electrodes in the envisioned sensor, it is crucial that the opposite electrodes from the IDTs are not cross-connected, however, this becomes more challenging as the width/gap distance decreases. To prevent any electrical conductivity from the substrate below the IDTs, fused silica was used. For biocompatibility purposes, these fused silica samples were overgrown with an intrinsic diamond layer of 450 nm prior to the lithography steps. Both spin and spray seeded samples were tested for the photolithography process. However, since the titanium pattern tended to peel off in the spray seeded samples, most likely due to the relatively high roughness, spin seeded samples were used for the fabrication of the electrodes.

In the first attempts to fabricate the desired IDT pattern, the spin-coating and photolithography parameters were based on experience in the

research group (31). For spin coating of the photoresist, a spin rate of 4000 rpm was used for 40 s. Subsequently, the sample was pre-baked for 60 s at 150 °C and post-baked for 60 s at 100 °C after 60 s of exposure to UV light. The sample was left in developer for 30 s. After the lithography process, a titanium layer of 50 nm was sputtered, followed by a lift-off step in acetone overnight. The results were not promising as the metal was still present in between the electrodes in some areas while in other areas the metal completely vanished (**Figure 4A**).

Based on this, the lift-off procedure was performed in a stepwise manner with ultrasonication instead of passive overnight dissolution. This resulted in a better pattern of the IDTs, however, the metal still peeled off, leading to disruptions in the electrodes (**Figure 4B**). Since fused silica is a thermal insulator with a conductivity of only 1.38 W/m$^{o}$K at 25 °C (32), the pre-and post- baking times were subsequently increased to 80 s. This gave rise to better IDTs, however, still, some impurities were seen in the electrode regions (**Figure 4C**).

Based on this finding, ozone treatment was performed prior to the metal deposition, as this creates an oxygen-terminated surface which is advantageous for titanium adhesion (33). This addition yielded better lift-off results in the IDT finger region. Nevertheless, because the mask was the same size as the substrates, the edge effect, i.e. spin-coated photoresist being thicker at the edges, was visible on the side electrodes of the IDTs (**Figure 4D**). To overcome this edge effect, the same photolithography and lift-off procedures were performed on larger substrates, which successfully translated into IDTs with a width and gap distance of 80 µm without any interconnections (**Figure 4E, F**).

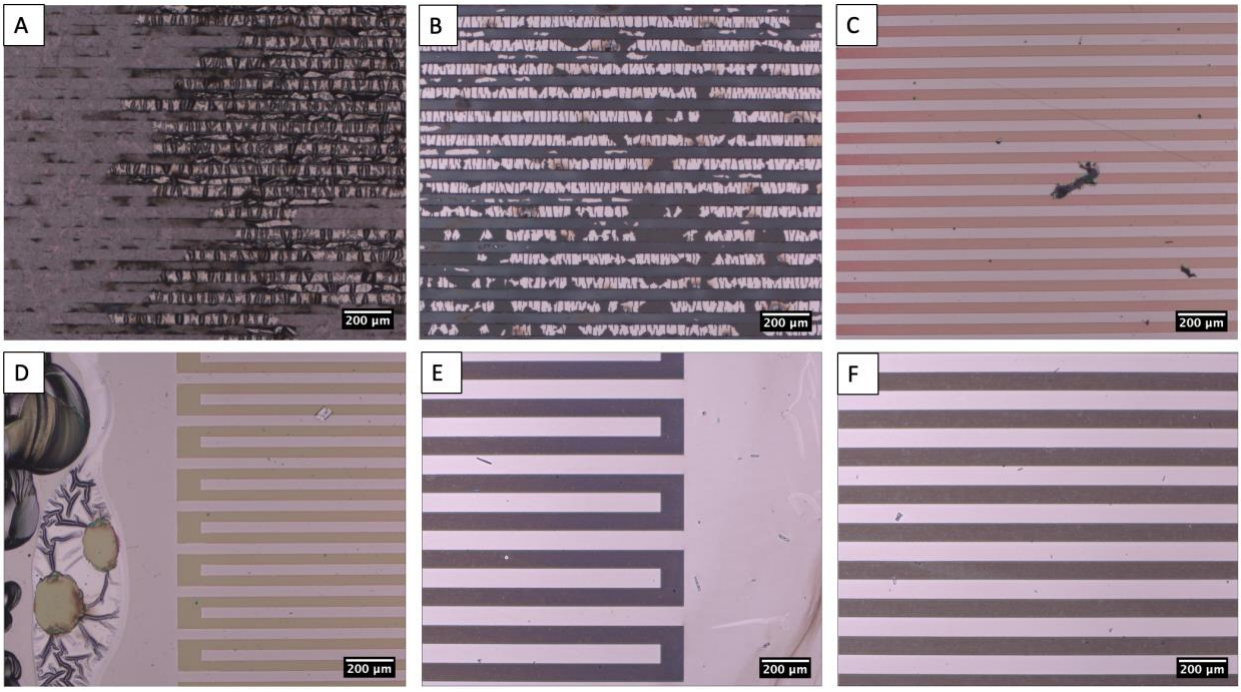


**Figure 4: Optimization of photolithography conditions.** The starting conditions of the photolithographic process were the following. The photoresist was spin-coated at 4000 rpm for 40 s. Subsequently, the sample was pre-baked for 60 s at 150 °C, followed by 60 s of exposure to UV light, and post-baking for 60 s at 100 °C. After the lithographic procedure, a titanium layer of 50 nm was sputtered and lift-off was performed overnight in acetone (A). Subsequently, the parameters were optimized one by one. First of all, lift-off overnight was changed to a stepwise lift-off procedure with 5 s ultrasonication (B). The pre-and post-baking times were enhanced by 20 s (C). Due to the sizes of the substrate and the mask, the edge effect was observed (D). After increasing the size of the substrates, titanium IDTs with a width/gap distance of 80 µm were successfully made (E and F).

*B-doped diamond IDTs* – In a second approach to make IDTs for the envisioned sensor, ink-jet printing was used to selectively seed nanodiamonds in the pattern of the IDTs followed by B-doped diamond growth in these regions. In a first attempt, this resulted in B-doped diamond IDTs, however, due to spontaneous B-doped diamond growth in the unseeded area, the whole surface was electrically conductive, which was undesired for the envisioned application. In the second attempt, the diamond growth run was significantly shorter, in order to create a thinner film and thereby prevent spontaneous growth. Nevertheless, again spontaneous diamond growth was observed in the non-seeded areas (**Figure 5**). Since the width and gap distances of these IDTs were set to 250 µm and 150 µm respectively, this might be due to the presence of scattered diamond particles around the printed areas due to the splashing of inferior inks, resulting in continuous diamond film formation (34).

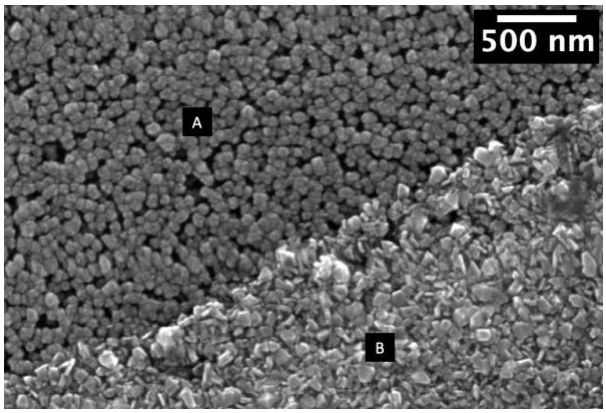


**Figure 5: SEM image of B-doped diamond IDTs.** The interface between the non-seeded (A) and ink-jet seeded (B) area of B-doped diamond IDTs shows the undesired diamond formation in the non-seeded area.

However, no diamond grains were seen with SEM, indicating that $CF_4$ cleaning possibly induced a suitable surface for spontaneous diamond growth. To investigate this, substrates cleaned with $O_2$ plasma, $CF_4$ plasma, and ozone treatment as well as a non-cleaned substrate were exposed to the same diamond growth conditions as used for the B-doped IDTs (**Figure 5**). From **Figure 6** it is visible that a diamond-like layer had formed on the $O_2$- and $CF_4$-treated substrate, while nothing was observed on the ozone and non-treated substrates. As expected, based on these results, no peaks were visible in the Raman spectra of the ozone and non-treated substrates, indicating the absence of any diamond-like phase (**Supplementary figure 5 and 6).** Nevertheless, the presence of pure diamond could also not be confirmed through Raman spectroscopy on the $O_2$- and $CF_4$-treated substrates (**Supplementary figure 7 and 8**). Instead of the $sp^3$ peak at 1332 $cm^{-1}$, characteristic for pure diamond, two peaks at 1350 $cm^{-1}$ and 1580 $cm^{-1}$ were observed. These peaks are commonly known as the G and D peaks and are related to the presence of $sp^2$ containing diamond-$\pi$ bonds, indicating the presence of non-diamond carbon (18). This might be a combined effect of the non-seeded substrates, the fact that the grown diamond layer is too thin, which leads to a scarce amount of diamond phase, and the laser wavelength used to excite in Raman spectroscopy. To rule out the effect of the last two factors, a thicker layer of diamond needs to be deposited on non-seeded substrates, cleaned with the different techniques, using the same deposition conditions, and the laser wavelength used to record the Raman spectra needs to be adjusted (35).

To unravel the mechanism behind the formation of the non-diamond carbon film on $O_2$- and $CF_4$-treated substrates, a more in-depth analysis of the surface is needed as it is known that surface morphology plays a major role in the nucleation density and subsequent diamond growth (36). In literature, an increased diamond growth rate has been reported with increased roughness of the substrate (37). To investigate if $O_2$ and $CF_4$ cleaning induce a rougher and therefore more suitable surface for spontaneous diamond growth compared to ozone treatment, AFM needs to be performed after the cleaning procedures. Moreover, X-ray photoelectron spectroscopy (XPS) can be used to determine and compare the surface chemistry changes induced by the various cleaning methods and relate these to the observed spontaneous growth.

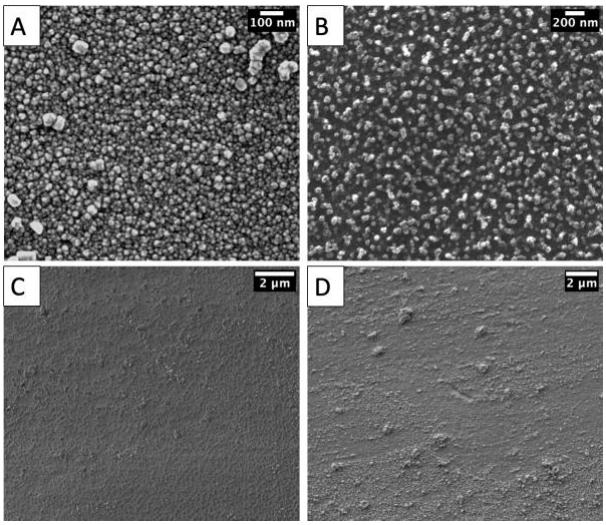


**Figure 6: SEM images of differently cleaned non-seeded substrates after BNCD growth.** Spontaneous non-diamond carbon film formation was observed in $O_2$ (A) and $CF_4$ (B) cleaned substrates. No diamond was observed in ozone-treated (C) and non-treated substrates (D).

*Printed conductive IDTs* – For these electrodes, samples of the spin seeded intrinsic diamond were used. On top of this, the IDT pattern was printed in silver-based conductive ink. This resulted in IDTs with a width/gap distance of 440 µm/150 µm (**Figure 7**). However, because the IDTs were too thick, it was not possible to make the flow cell watertight after their incorporation. Moreover, these IDTs oxidized immediately after contact with the electrolyte, giving rise to undesired noise, in the obtained spectra.

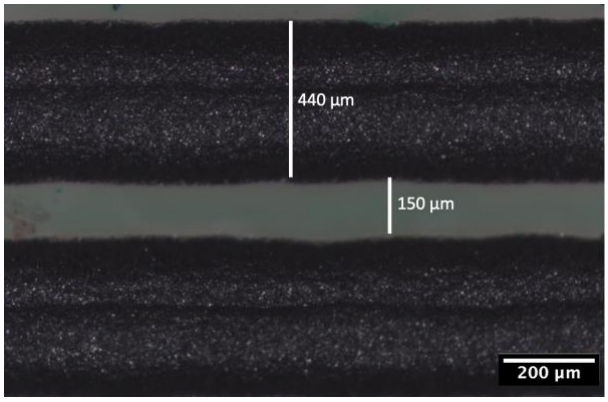


**Figure 7: Optical microscopy image of the central region of the conductive IDTs printed on an intrinsic diamond film.**

**Electrochemical measurements**

*B-doped diamond electrode* – CV was performed on a concentration range of vanillin (4-hydroxy-3-methoxybenzaldehyde) in 0.01 M PBS as an initial investigation of the electrochemical properties of the electrode as well as its performance in the setup.

In the presence of water molecules, 4-hydroxy-3-methoxybenzaldehyde is oxidized resulting in a loss of 2 electrons that contribute to the current flow between the electrolyte and the diamond electrode (38). Since no reduction peak was observed in the cyclic voltammograms, only the potential range of 0.2 V to 1.2 V was included in the graph (**Figure 8A**). The oxidation peak of vanillin was situated at 0.637 V, which is similar to literature (39). As expected, an increase in the extracted peak current ($I_p$) was seen with the increasing concentration of the analyte. This relationship can be described by the exponential function $I_p = 9.9217\, e^{32.534x}$ ($R^2$ = 0.9703), where $x$ is the concentration of vanillin.

The effects of vanillin on the impedance of the system were also studied using EIS. The resulting Nyquist plots (**Figure 8B**), show the formation of a semi-circle. Based on this, it can be assumed that vanillin has the tendency to be adsorbed on the B-doped diamond surface. Due to this adsorption, i.e. adhesion of vanillin to the diamond surface, the electroactive compound will contribute to the electric charge transport across the electrode-electrolyte interface.

The equivalent circuit that can be used to model these semicircular spectra is a Randles circuit (40). This is one of the simplest and most commonly used circuit models for EIS spectra. This circuit is composed of a solution resistance $R_s$ in series with a parallel combination of a charge transfer resistance $R_{ct}$ and a double layer capacitor $C_{dl}$, representing the electrode capacitance. In the obtained Nyquist plots, the solution resistance can be found at the high-frequency intercept, i.e. close to the origin, with the $x$-axis. The diameter of the obtained semi-circles allows one to estimate the charge transfer resistance. From the graphs, it is visible that the solution resistance is highly similar for each of the concentrations of vanillin while the charge transfer resistance decreases with the increasing concentration of vanillin. This observation is in line with the cyclic

voltammograms (**Figure 8A**), since a decrease in impedance means a higher conductivity and thus a higher extracted peak current with increasing concentrations of vanillin.

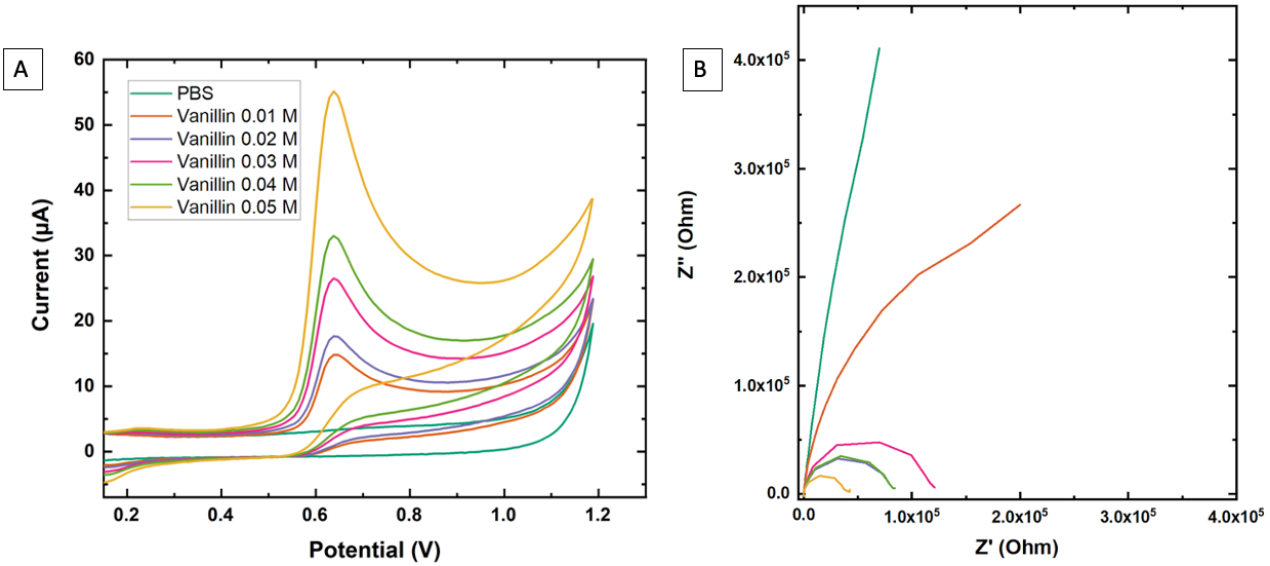


**Figure 8: Electrochemical measurements of vanillin in bare boron-doped diamond electrodes.** The cyclic voltammograms show a linear relationship between the extracted peak current and the concentration of vanillin (A). The Nyquist plots obtained after EIS measurements show an increase in impedance with increasing concentration of vanillin (B).

As the goal of the envisioned sensor is to monitor the growth of a cyanobacterial biofilm, *Saccharomyces cerevisiae*, i.e. baker's yeast, was used to investigate the influence of a biofilm, formed on the surface of the B-doped diamond electrode, on the extracted current. Again, both cyclic voltammograms and electrochemical impedance spectra were recorded with increasing concentrations of yeast (**Figure 9**).

In this case, the resulting cyclic voltammograms do not show an increase in the extracted peak current with increasing yeast concentration (**Figure 9A**). Instead, the extracted peak currents of all concentrations, except for 0.01 M, which is likely to be a faulty measurement due to connection problems, are in the same range. Since the charge transfer processes contributing to the extracted peak current take place at the electrode interface, this might indicate that the surface is completely saturated with yeast cells at all tested concentrations.

Another interesting feature of the recorded voltammograms is the shift in peak potential (**Figure 9B**). It can be seen that the peak positions shift to a lower peak potential with increasing yeast concentration. This might be due to the process of an increasing yeast concentration leading to an increase in the pH of the electrolyte, resulting in the observed decrease in peak potential. This relationship between pH and the peak potential was also observed by *Acevedo et al.* (41) in their electrochemical determinations of yeast.

Concerning the EIS measurements on the yeast concentration range, again, an increase in conductivity, i.e. a decrease in the impedance, is observed with increasing yeast concentration (**Figure 9C**). This is in line with the findings of *Gonzalez-Aravena et al.* (23), who carried out electrochemical measurements on different thicknesses of biofilms, and observed an increase in extracted current with thicker biofilms on the electrode.

It is also visible in the resulting Nyquist plots, that there is a tendency for forming a semicircle, especially at the high-frequency end of the graph. Nevertheless, based on the total shape of the graph, it is probable that the plots consist of multiple convoluted semicircles, however, the circuit modeling of such complex data falls outside the scope of this paper.

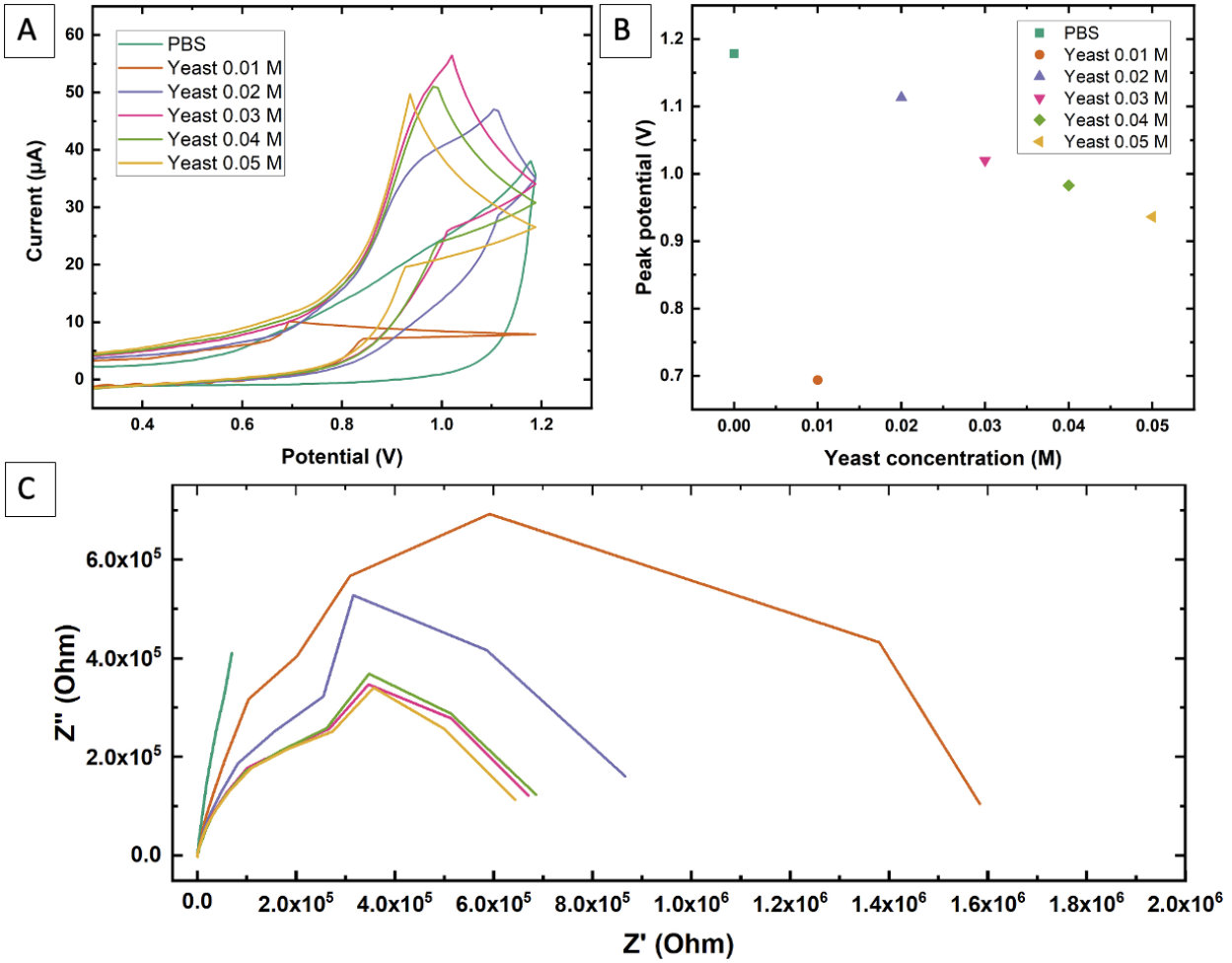


**Figure 9: Electrochemical measurements of *Saccharomyces cerevisiae* on bare boron-doped diamond electrodes.** The obtained cyclic voltammograms do not show an increase in extracted peak current with increasing concentration of yeast (A). Instead, a shift in peak potential to lower values is observed with increasing concentration of yeast (B). The Nyquist plots obtained after EIS show an increased conductivity with an increasing yeast concentration (C).

*Titanium IDTs on NCD film* – Since usually IDTs are used for EIS measurements of growing cells, the envisioned sensor contains such electrodes instead of B-doped diamond film electrodes. Within the limited time frame of this internship, only photolithography gave rise to successful titanium IDT electrodes. For this reason, EIS was carried out on the same concentration range of yeast cells as used in the previous section on these titanium IDTs. As expected, based on the previous section, the resulting spectra (**Figure 10**) show again an increase in conductivity or a decrease in impedance with increasing yeast concentration. Nevertheless, the difference between the different concentrations is smaller, indicating that the developed electrode might not be as accurate in the determination of the yeast concentration. This might be because the working surface area of this type of electrode is significantly smaller compared to the working surface area of the B-doped diamond electrodes. However, to investigate the quantitative aspects of the developed sensor, extensive equivalent circuit modeling and more testing are needed, which falls outside the scope of this internship.

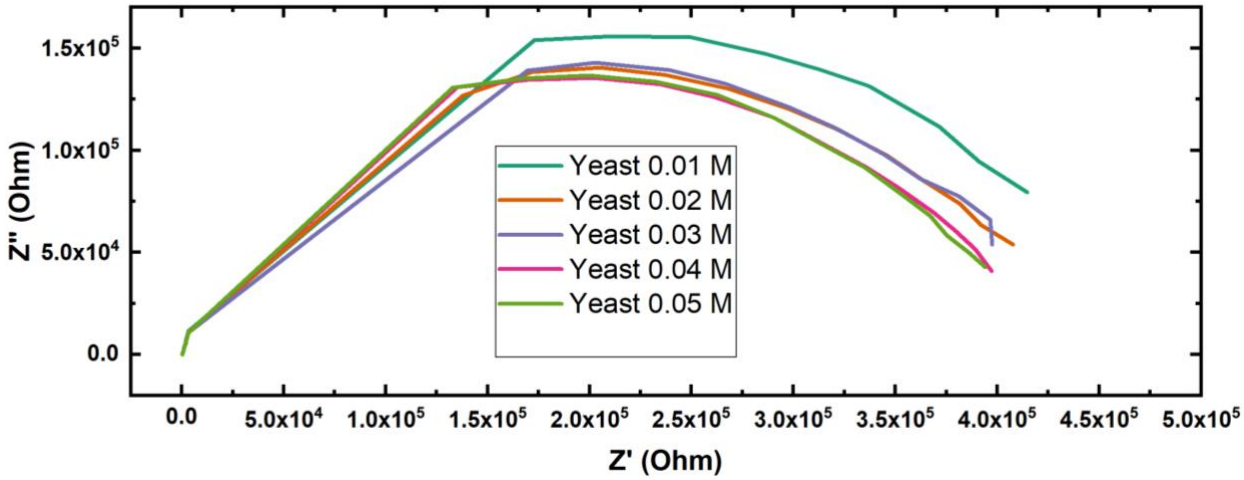


**Figure 10: Nyquist plots of different concentrations of *Saccharomyces cerevisiae* on the titanium IDTs on an intrinsic diamond layer.** Similar to the measurements with the bare boron-doped diamond electrodes, a decrease in impedance is observed with increasing concentration of yeast.

## CONCLUSION

In this work, the development of a new, alternative impedance-based sensor to monitor (cyano)bacterial growth was described. As a proof of principle, baker's yeast was used because of its biofilm-forming behavior. Different approaches to form the envisioned IDT electrodes were investigated. However, due to the limited time frame of the internship, only titanium IDTs on intrinsic diamond were successfully created. The results of EIS measurements with these electrodes showed an increasing conductivity with increasing yeast concentration. This probably means that yeast contributes to the electrical charge transfer between the electrolyte and the electrode, however, the mechanism behind this observation is still to be investigated in further research, potentially through extensive equivalent circuit modeling. The electrochemical measurements on vanillin and yeast with B-doped diamond films without IDTs proved that this type of electrode also works, which might present an easier and less laborious type of electrode. However, in future work, both electrodes must be evaluated in terms of sensitivity, reproducibility, and the ability to monitor cyanobacterial biofilm evolution over time.

With the approach to make B-doped IDTs through selective ink-jet printing of nanodiamond seeds, it was found that non-diamond carbon can spontaneously grow on non-seeded surfaces when cleaned with $O_2$ or $CF_4$ plasma. This might present a breakthrough since it would mean that surface pre-treatment of samples prior to diamond deposition can be circumvented. Nevertheless, the mechanism behind this observation is still to be investigated in depth by surface-sensitive analytical techniques like AFM and XPS.

The presented results provide the very first cornerstones towards the development of a new sensor concept to monitor (cyano)bacterial biofilm formation, which is crucial to support and stimulate the increasing number of applications of these bacterial strains in the biotechnological industry.

**REFERENCES**

1. Sánchez-Baracaldo P, Cardona T. On the origin of oxygenic photosynthesis and Cyanobacteria. New Phytologist. 2020;225(4):1440–6.

2. Abed RMM, Dobretsov S, Sudesh K. Applications of cyanobacteria in biotechnology. J Appl Microbiol. 2009 Jan;106(1):1–12.

3. BioHydrogen [Internet]. [cited 2022 May 31]. Available from: https://link.springer.com/book/10.1007/b102384

4. Yadav A, Link to external site this link will open in a new window, Maertens L, Meese T, Nieuwerburgh FV, Link to external site this link will open in a new window, et al. Genetic Responses of Metabolically Active Limnospira indica Strain PCC 8005 Exposed to γ-Radiation during Its Lifecycle. Microorganisms. 2021;9(8):1626.

5. Janssen PJD, Lambreva MD, Plumeré N, Bartolucci C, Antonacci A, Buonasera K, et al. Photosynthesis at the forefront of a sustainable life. Frontiers in Chemistry [Internet]. 2014 [cited 2022 Jan 26];2. Available from: https://www.frontiersin.org/article/10.3389/fchem.2014.00036

6. Hendrickx L, De Wever H, Hermans V, Mastroleo F, Morin N, Wilmotte A, et al. Microbial ecology of the closed artificial ecosystem MELiSSA (Micro-Ecological Life Support System Alternative): Reinventing and compartmentalizing the Earth's food and oxygen regeneration system for long-haul space exploration missions. Research in Microbiology. 2006 Jan 1;157(1):77–86.

7. Loutfi H, Pellen F, Le Jeune B, Lteif R, Kallassy M, Le Brun G, et al. Real-time monitoring of bacterial growth kinetics in suspensions using laser speckle imaging. Sci Rep. 2020 Jan 15;10(1):408.

8. O'Toole DK. Methods for the direct and indirect assessment of the bacterial content of milk. J Appl Bacteriol. 1983 Oct;55(2):187–201.

9. Ferrari A, Lombardi S, Signoroni A. Bacterial colony counting by Convolutional Neural Networks. In: 2015 37th Annual International Conference of the IEEE Engineering in Medicine and Biology Society (EMBC). 2015. p. 7458–61.

10. van Duuren JBJH, Müsken M, Karge B, Tomasch J, Wittmann C, Häussler S, et al. Use of Single-Frequency Impedance Spectroscopy to Characterize the Growth Dynamics of Biofilm Formation in Pseudomonas aeruginosa. Sci Rep. 2017 Jul 12;7(1):5223.

11. Kang J, Kim T, Tak Y, Lee JH, Yoon J. Cyclic voltammetry for monitoring bacterial attachment and biofilm formation. Journal of Industrial and Engineering Chemistry. 2012 Mar 25;18(2):800–7.

12. Barsoukov E, Macdonald JR, editors. Impedance Spectroscopy Theory, Experiment, and Applications. In: Impedance Spectroscopy [Internet]. 1st ed. Wiley; 2005 [cited 2022 May 31]. Available from: https://onlinelibrary.wiley.com/doi/10.1002/0471716243.fmatter

13. Procházka V, Matějka R, Ižák T, Szabó O, Štěpanovská J, Filová E, et al. Nanocrystalline diamond-based impedance sensors for real-time monitoring of adipose tissue-derived stem cells. Colloids and Surfaces B: Biointerfaces. 2019 May 1;177:130–6.

14. Huang F, Xue L, Qi W, Cai G, Liu Y, Lin J. An ultrasensitive impedance biosensor for Salmonella detection based on rotating high gradient magnetic separation and cascade reaction signal amplification. Biosens Bioelectron. 2021 Mar 15;176:112921.

15. Abdelrasoul GN, Anwar A, MacKay S, Tamura M, Shah MA, Khasa DP, et al. DNA aptamer-based non-faradaic impedance biosensor for detecting E. coli. Anal Chim Acta. 2020 Apr 22;1107:135–44.

16. Furst AL, Francis MB. Impedance-Based Detection of Bacteria. Chem Rev. 2019 Jan 9;119(1):700–26.

17. Kim G, Morgan M, Hahm BK, Bhunia A, Mun JH, Om AS. Interdigitated microelectrode based impedance biosensor for detection of salmonella enteritidis in food samples. J Phys: Conf Ser. 2008 Mar;100(5):052044.

18. Macpherson JV. A practical guide to using boron doped diamond in electrochemical research. Phys Chem Chem Phys. 2015 Feb 7;17(5):2935–49.

19. Macpherson JV. A practical guide to using boron doped diamond in electrochemical research. Phys Chem Chem Phys. 2015 Jan 21;17(5):2935–49.

20. Optical and electrical properties of boron doped diamond thin conductive films deposited on fused silica glass substrates - ScienceDirect [Internet]. [cited 2022 May 7]. Available from: https://www.sciencedirect.com/science/article/pii/S0169433216313940

21. Rouzbahani R, Nicley SS, Vanpoucke DEP, Lloret F, Pobedinskas P, Araujo D, et al. Impact of methane concentration on surface morphology and boron incorporation of heavily boron-doped single crystal diamond layers. Carbon. 2021 Feb 1;172:463–73.

22. Izak T, Krátká M, Kromka A, Rezek B. Osteoblastic cells trigger gate currents on nanocrystalline diamond transistor. Colloids Surf B Biointerfaces. 2015 May 1;129:95–9.

23. Gonzalez-Aravena AC, Yunus K, Zhang L, Norling B, Fisher AC. Tapping into cyanobacteria electron transfer for higher exoelectrogenic activity by imposing iron limited growth. RSC Adv. 2018 May 30;8(36):20263–74.

24. Ali HS, Abdullah AA, Pınar PT, Yardım Y, Şentürk Z. Simultaneous voltammetric determination of vanillin and caffeine in food products using an anodically pretreated boron-doped diamond electrode: Its comparison with HPLC-DAD. Talanta. 2017 Aug 1;170:384–91.

25. Botstein D, Fink GR. Yeast: An Experimental Organism for 21st Century Biology. Genetics. 2011 Nov;189(3):695–704.

26. Lakna. Difference Between Yeast and Bacteria [Internet]. Pediaa.Com. 2018 [cited 2022 Jun 4]. Available from: https://pediaa.com/difference-between-yeast-and-bacteria/

27. Reynolds TB, Fink GR. Bakers' Yeast, a Model for Fungal Biofilm Formation. Science. 2001 Feb 2;291(5505):878–81.

28. Bruno L, Di Pippo F, Antonaroli S, Gismondi A, Valentini C, Albertano P. Characterization of biofilm-forming cyanobacteria for biomass and lipid production. J Appl Microbiol. 2012 Nov;113(5):1052–64.

29. Thomas ELH, Gines L, Mandal S, Klemencic GM, Williams OA. A simple, space constrained NIRIM type reactor for chemical vapour deposition of diamond. AIP Advances. 2018 Mar;8(3):035325.

30. Law KY. Definitions for Hydrophilicity, Hydrophobicity, and Superhydrophobicity: Getting the Basics Right. J Phys Chem Lett. 2014 Feb 20;5(4):686–8.

31. Rouzbahani Bayatani R. Heavily boron-doped CVD diamond for pseudo-vertical Schottky barrier diodes. IIOimport [Internet]. 2021 May [cited 2022 May 14]; Available from: https://imec-publications.be/handle/20.500.12860/37121

32. Material of the Month: Fused Silica [Internet]. Swift Glass. 2017 [cited 2022 May 23]. Available from: https://www.swiftglass.com/blog/material-month-fused-silica/

33. Motochi I, Makau NW, Amolo GO. Metal–semiconductor ohmic contacts: An ab initio Density Functional Theory study of the structural and electronic properties of metal–diamond (111)-(1×1) interfaces. Diamond and Related Materials. 2012 Mar 1;23:10–7.

34. Chen YC, Tzeng Y, Davray A, Cheng AJ, Ramadoss R, Park M. Fabrication of diamond micro-structures by ink-jet printed diamond seeding and microwave plasma assisted chemical vapor deposition. Diamond and Related Materials. 2008 Apr 1;17(4):722–7.

35. Inzoli F, Dellasega D, Russo V, Ghezzi F, Passoni M. Early stages of diamond growth on substrates with different carbon diffusivity. Diamond and Related Materials. 2017 Nov 1;80:69–75.

36. Withanage S, Nanayakkara T, Wijewardena UK, Kriisa A, Mani RG. The role of surface morphology on nucleation density limitation during the CVD growth of graphene and the factors influencing graphene wrinkle formation. MRS Advances. 2019 Dec 1;4(61):3337–45.

37. Mallik AK, Binu SR, Satapathy LN, Narayana C, Seikh MM, Shivashankar SA, et al. Effect of substrate roughness on growth of diamond by hot filament CVD. Bull Mater Sci. 2010 Jun 1;33(3):251–5.

38. Sensitive and selective electrochemical detection of vanillin at graphene based poly (methyl orange) modified electrode - ScienceDirect [Internet]. [cited 2022 May 10]. Available from:

https://www.sciencedirect.com/science/article/pii/S2468217921000319

39. Shang L, Zhao F, Zeng B. Sensitive voltammetric determination of vanillin with an AuPd nanoparticles−graphene composite modified electrode. Food Chemistry. 2014 May 15;151:53–7.

40. Rosliza R, Nora'aini A, Wan Nik WB. Study on the effect of vanillin on the corrosion inhibition of aluminum alloy. J Appl Electrochem. 2010 Apr 1;40(4):833–40.

41. Acevedo Restrepo I, Blandón Naranjo L, Hoyos-Arbeláez J, Víctor Vázquez M, Gutiérrez Granados S, Palacio J. Electrochemical determination of Saccharomyces cerevisiae sp using glassy carbon electrodes modified with oxidized multi-walled carbon nanotubes dispersed in water –Nafion®. Current Research in Food Science. 2022 Jan 1;5:351–9.

*Acknowledgements* – NC greatly acknowledges prof. dr. Haenen and dr. Pobedinskas for the opportunity to execute this internship in the Wide Bandgap materials research group. Dr. Rouzbahani R. is thankfully acknowledged for being the promotor of this work and for the numerous AFM and SEM images. NC is thankful for all the help and input of Ahmed E., the daily supervisor of this internship. Ahmed E. is also thanked for providing access to Raman spectroscopy. Dr. Pobedinskas, dr. Rouzbahani R. and Ahmed E are gratefully acknowledged for their reviewing. NC is grateful for the help and input of prof. dr. An Hardy as a second examiner. NC would also like to thank dr. Braun (Empa, Switzerland) for his great help and input in the interpretation of the data of the electrochemical measurements and for reviewing. Verding P., from the research group of prof. dr. ir. Wim Deferme, is gratefully acknowledged for offering the opportunity to investigate spray seeding and ink-jet printed seeding in this thesis, as well as for the numerous SEM images he made. NC is grateful for the collaboration with Zalieckas J. (University of Bergen, Norway) on the conductive printed IDTs. The research group of prof. dr. Ronald Thoelen is acknowledged for providing the potentiostat used in this work. The logistic team at IMO is thanked for all their help with technical issues.

*Author contributions* – NC, AE, RR, and dr. Pobedinskas conceived and designed the research. NC performed experiments and data analysis. AE provided assistance with Raman spectroscopy. RR provided access to AFM and SEM. NC wrote the paper. All authors carefully edited the manuscript.

**SUPPLEMENTARY INFORMATION**

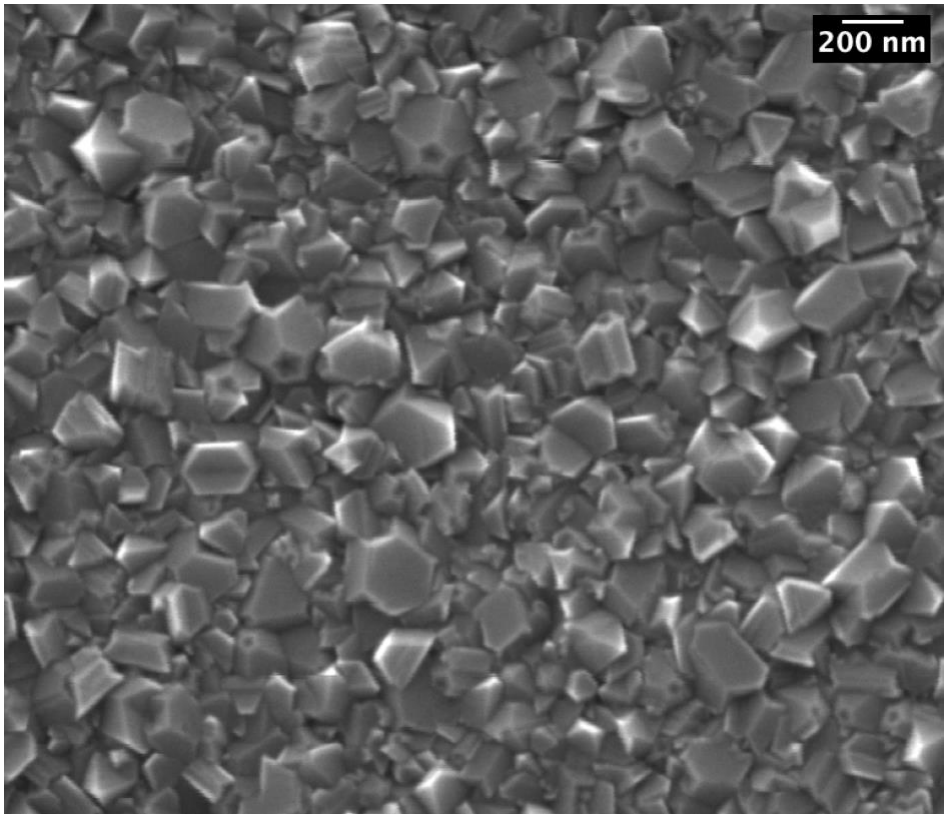


**Supplementary figure 1:** SEM image of the nanocrystalline boron-doped diamond film used for the fabrication of the BDD film electrodes. An average grain size of 261 nm was found.

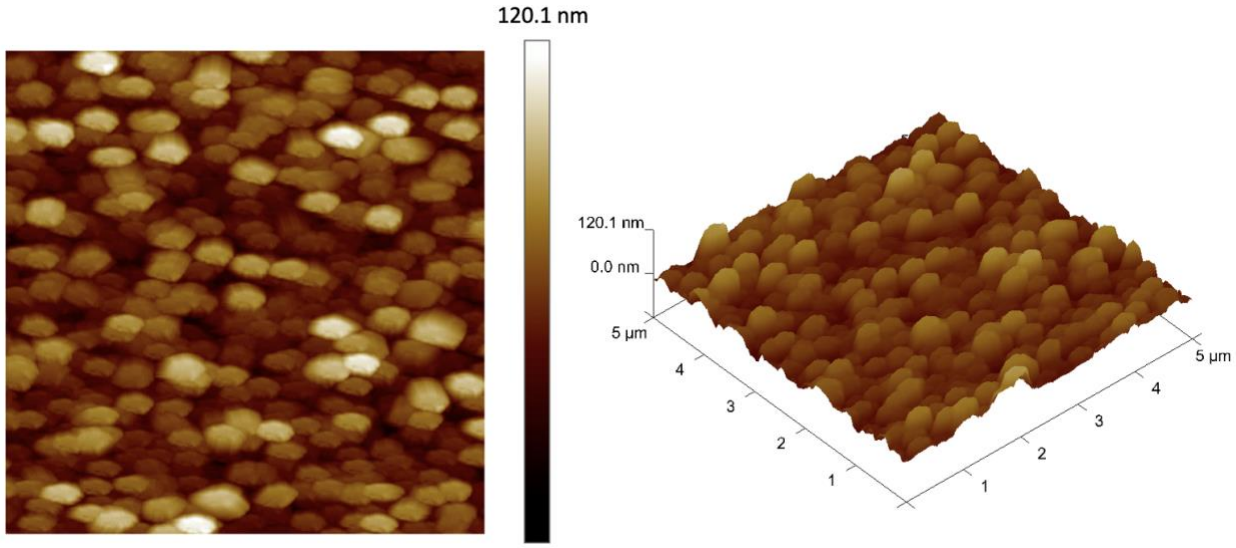


**Supplementary figure 2:** AFM images of the boron-doped diamond film used for the fabrication of the BDD electrode. An average surface roughness value of 10.4 nm was found.

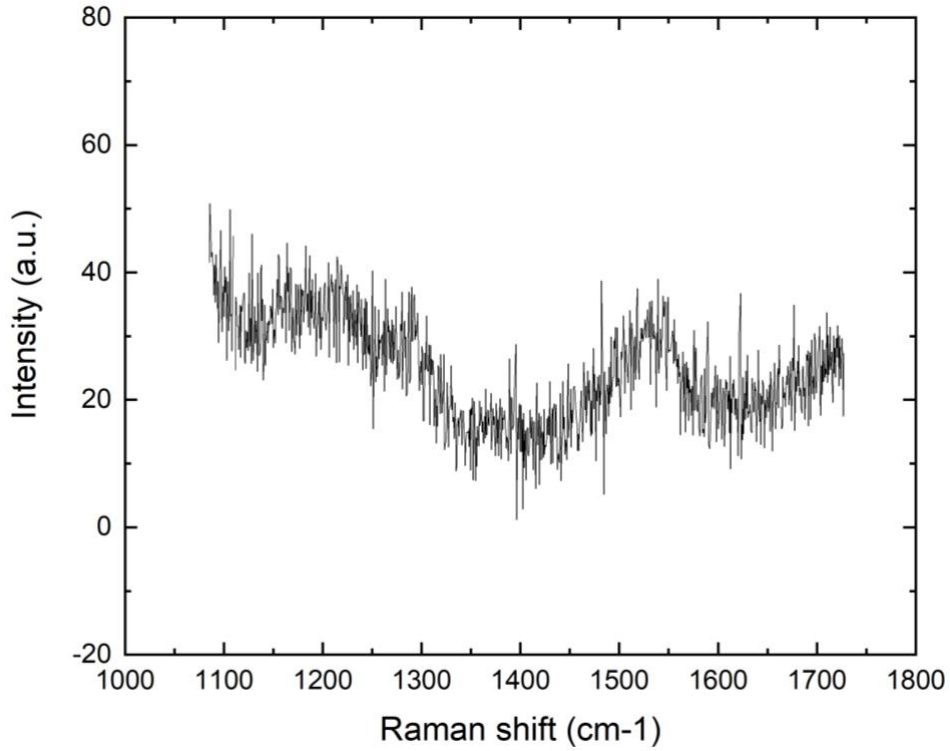


**Supplementary figure 3:** Raman spectrum of the BDD film used for the fabrication of the BDD film electrode. The peak at 1332 $cm^{-1}$ confirmed the presence of pure diamond in the film, and the broad peak at 1550 $cm^{-1}$ can be attributed to the presence of non-diamond carbons, which are $sp^2$ hybridized.

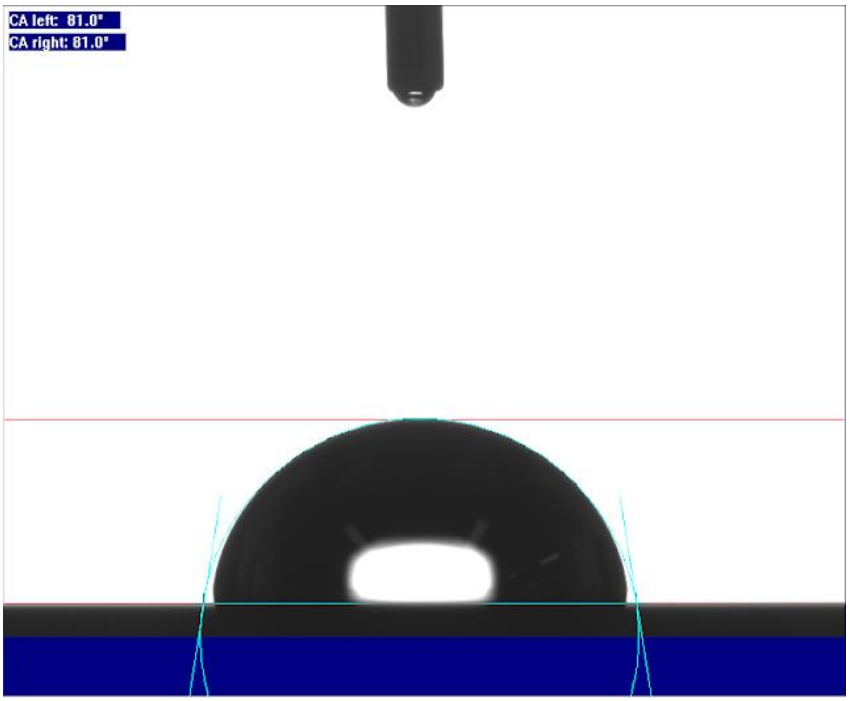


**Supplementary figure 4**: Contact angle measurements of the BDD film used for the fabrication of the BDD film electrode. The CA of 81° indicated the presence of a hydrophobic hydrogen-terminated surface.

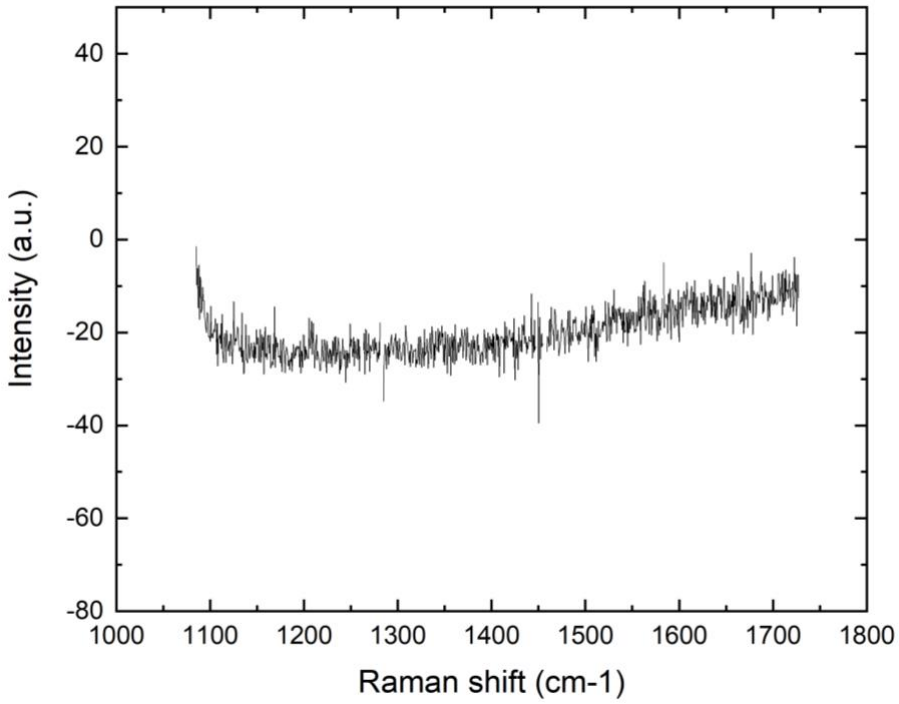


**Supplementary figure 5:** Raman spectrum of ozone treated sample after diamond deposition process without seeding. The spectrum shows no evidence of $sp^2$ or $sp^3$, indicating that no diamond is present.

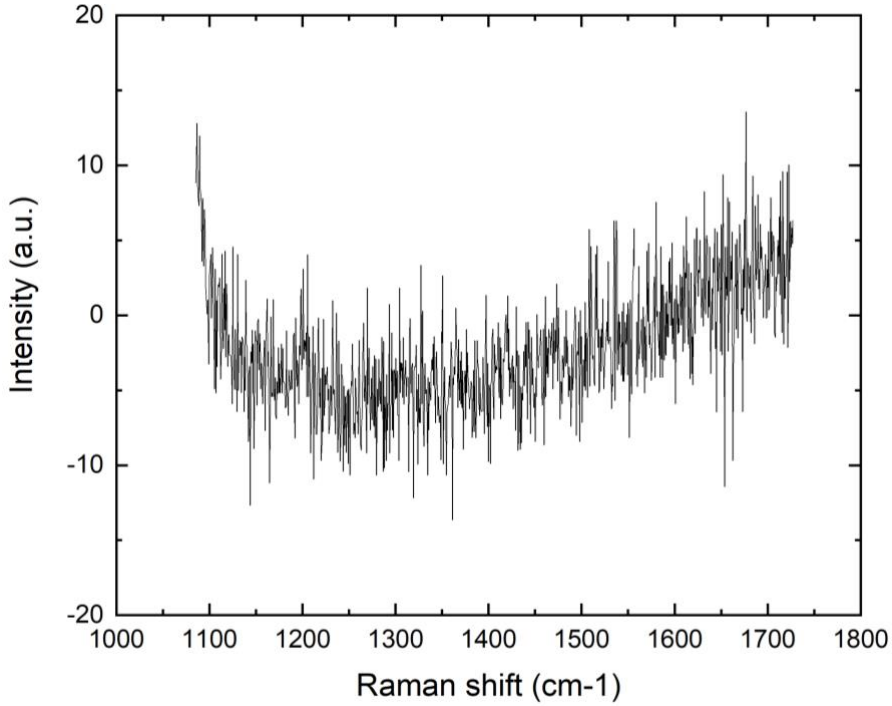


**Supplementary figure 6:** Raman spectrum of non-cleaned sample after diamond deposition without seeding. No peaks are observed in the spectrum, indicating the absence of $sp^2$ and $sp^3$ carbon.

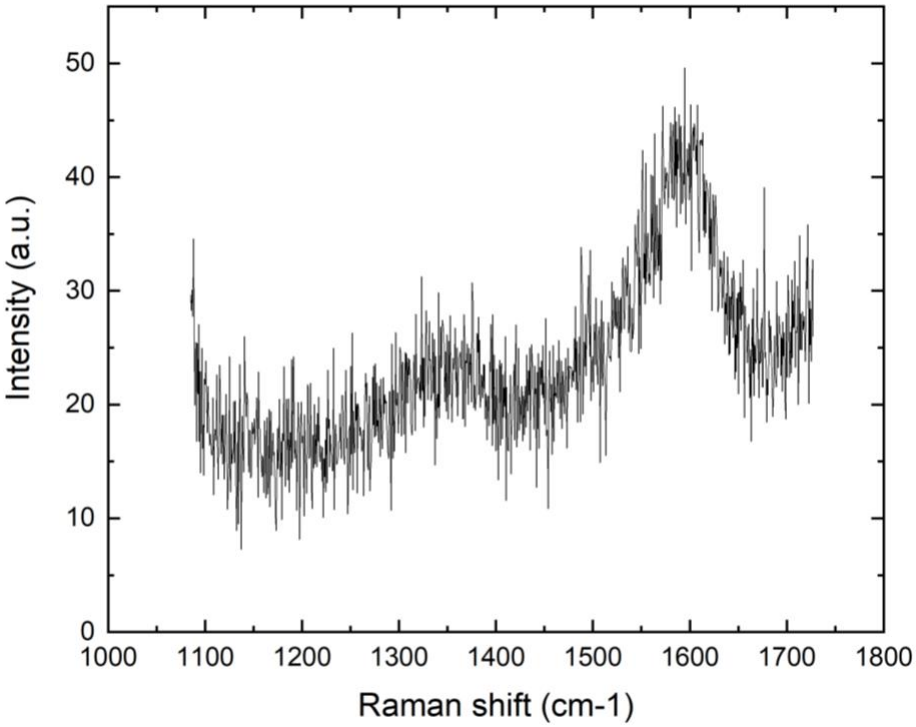


**Supplementary figure 7:** Raman spectrum of $O_2$ plasma cleaned substrate after diamond deposition without seeding. The peak at 1580 $cm^{-1}$ shows the presence of $sp^2$ carbon atoms.

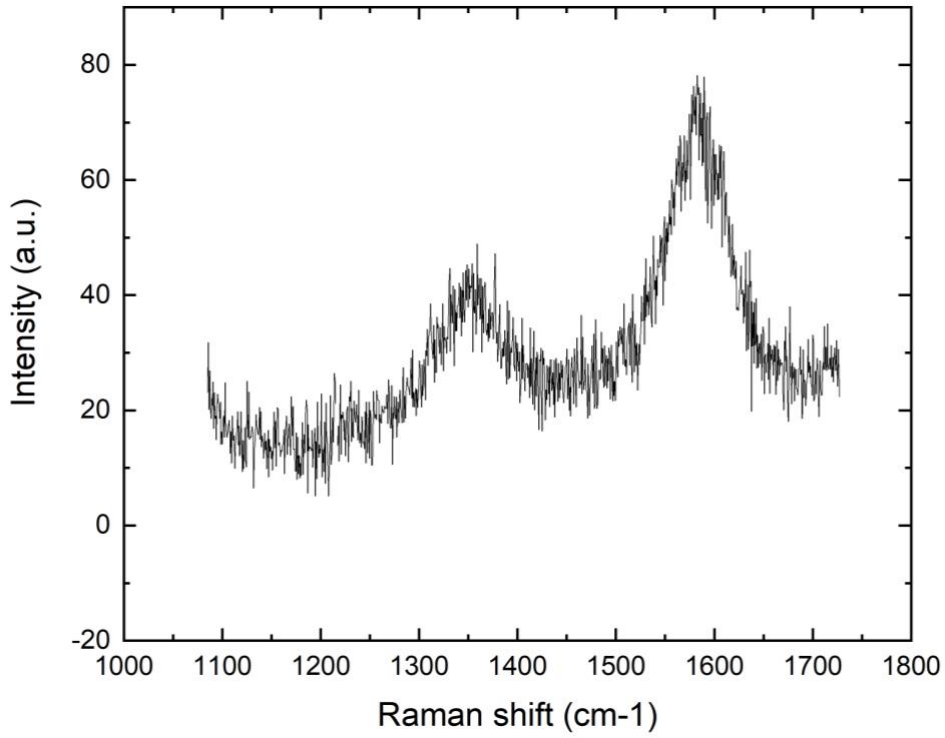


**Supplementary figure 8:** Raman spectrum of $CF_4$ plasma cleaned sample after diamond deposition process without seeding. The peaks at the 1350 $cm^{-1}$ and 1580 $cm^{-1}$ correspond to the G and D peaks produced by non-carbon diamond. These are a result of stretching of pairs of $sp^2$ sites (rings and chains) and the breathing mode of $sp^2$ rings, respectively.